# Tracking solid electrolyte interphase dynamics using operando fibre-optic infrared spectroscopy and multivariate curve regression

C. Leau[1,2,3], Y. Wang[1,2], C. Gervillié-Mouravieff[1,2], S. T. Boles[4], X. H. Zhang[5], S. Coudray[5], C. Boussard-Plédel[5], J.-M.Tarascon[1,2,3]*

[1]Chimie du Solide et de l'Énergie, UMR 8260, Collège de France, Paris, France.

[2]Réseau sur le Stockage Électrochimique de l'Énergie (RS2E), FR CNRS 3459, France.

[3]Sorbonne Université–Université Pierre-et-Marie-Curie Paris (UPMC), Paris, France.

[4]Department of Energy and Process Engineering, Faculty of Engineering, Norwegian University of Science and Technology (NTNU), Trondheim, Norway.

[5]Institut des Sciences Chimiques de Rennes (ISCR), UMR 6226, Univ. Rennes, CNRS, Rennes, France.

*Corresponding author: jean-marie.tarascon@college-de-france.fr

## Supplementary: Solvent Reference Spectra

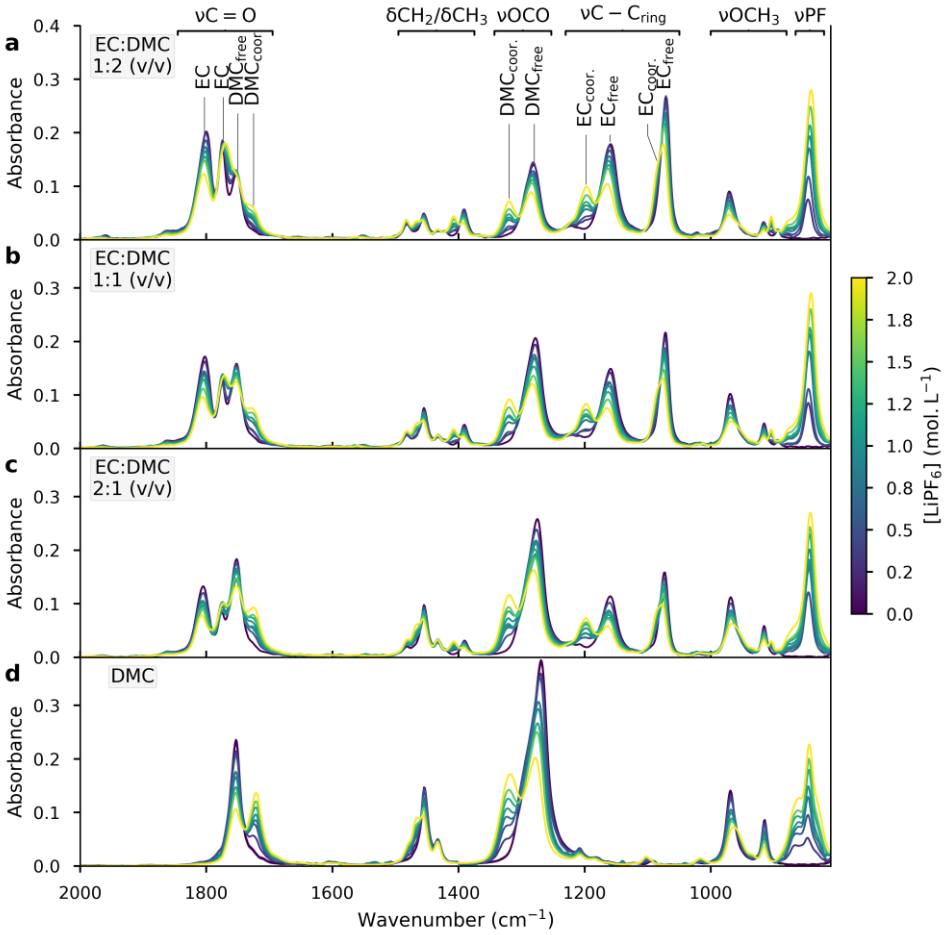


Supplementary Fig. 1. Electrolyte calibration reference spectra, with $LiPF_6$ concentration from 0.0 M to 2.0 M, using EC:DMC as solvent with ratio of **a,** 1:2; **b,** 1:1 and **c,** 2:1 (v/v); **d,** using DMC as solvent.

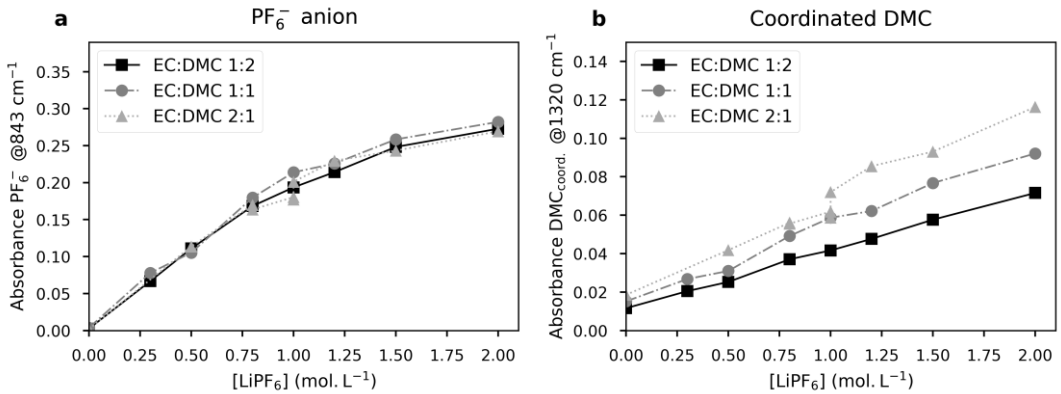


Supplementary Fig. 2. Electrolyte spectrum evolution as changing $LiPF_6$ concentration in EC:DMC at various ratio (v/v), tracked by : **a,** the $PF6^-$ anion at 843 $cm^{-1}$, **b,** the band associated to salt-coordinating DMC at 1320 $cm^{-1}$.

As depicted in Supplementary Fig. 2a, the $PF_6^-$ anion band at 843 $cm^{-1}$ appears when salt is added to the solvent, and its intensity grows when increasing the concentration. However, contrary to the coordinated solvent bands such as reported in Supplementary Fig. 2b, which displays a steady linear increase with increasing concentration, the anion band deviates from Beer-Lambert's law above 1 $mol.L^{-1}$. Therefore, the analysis range was limited to 900 $cm^{-1}$ to exclude this band from the MCR-ALS.

## Supplementary: Pictures of the experimental setup

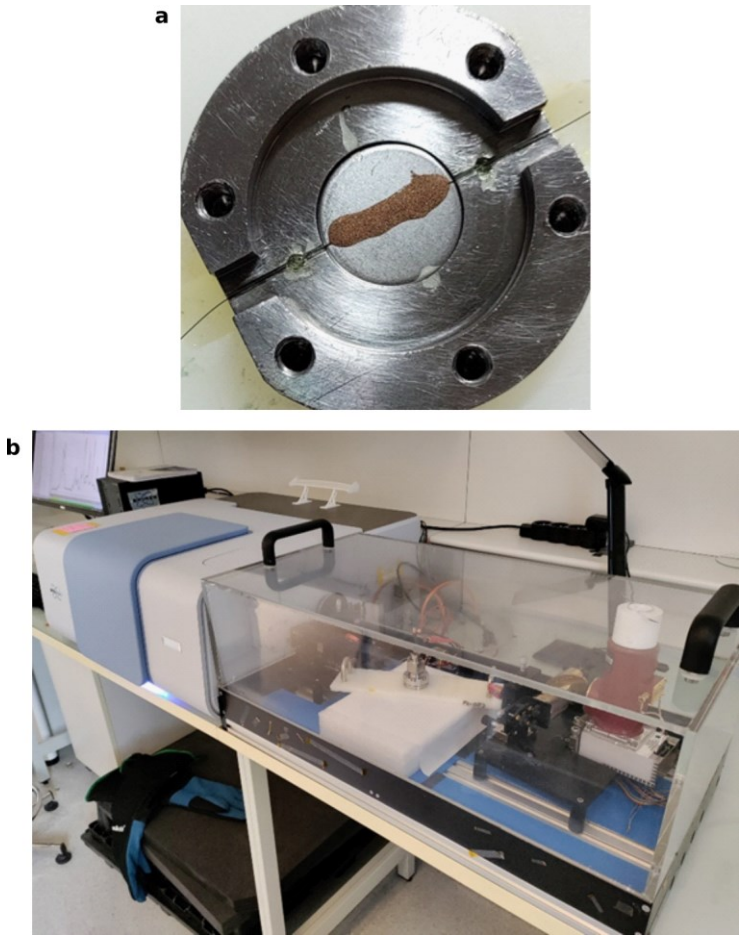


Supplementary Fig. 3. **a** Bottom part of the operando cell, the electrode material covers the central part of the fibre (here copper/PVDF). **b** FTIR spectrometer (left) with a fibre testing custom module (right).

## Supplementary: Capacity of the cells presented – Cu-PVDF | Various electrolytes | Li Metal

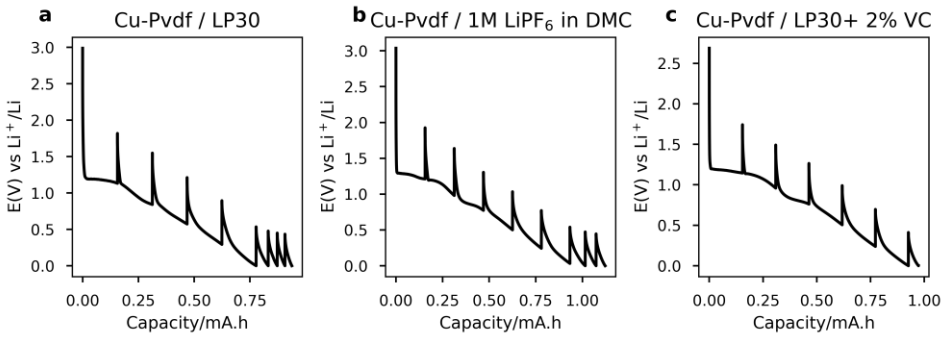


Supplementary Fig. 4. Reduction capacity for three electrolytes (**a** LP30, **b** 1M $LiPF_6$ in DMC, and **c** LP30+ 2 wt.% VC). The electrode material is Cu-PVDF, the GITT protocol is applied with a current of 206 µA.

An electrode consisting of 90 mg of metallic copper corresponds to a copper volume of $10^{-2}$ $cm^3$ or $10^{10}$ $\mu m^3$. Considering particles of diameter 100 µm, the individual particale volume is $5 \times 10^5$ $\mu m^3$, corresponding to $2 \times 10^4$ particles in the electrode. Consequently, the resulting electrode surface is 6 $cm^2$. Ultimately, the order of magnitude of surfacic current applied is $3 \times 10^{-2}$ $mA/cm^2$.

## Supplementary: X-ray photoelectron spectroscopy (XPS) of Cu-Pdvf and TAS fibres samples

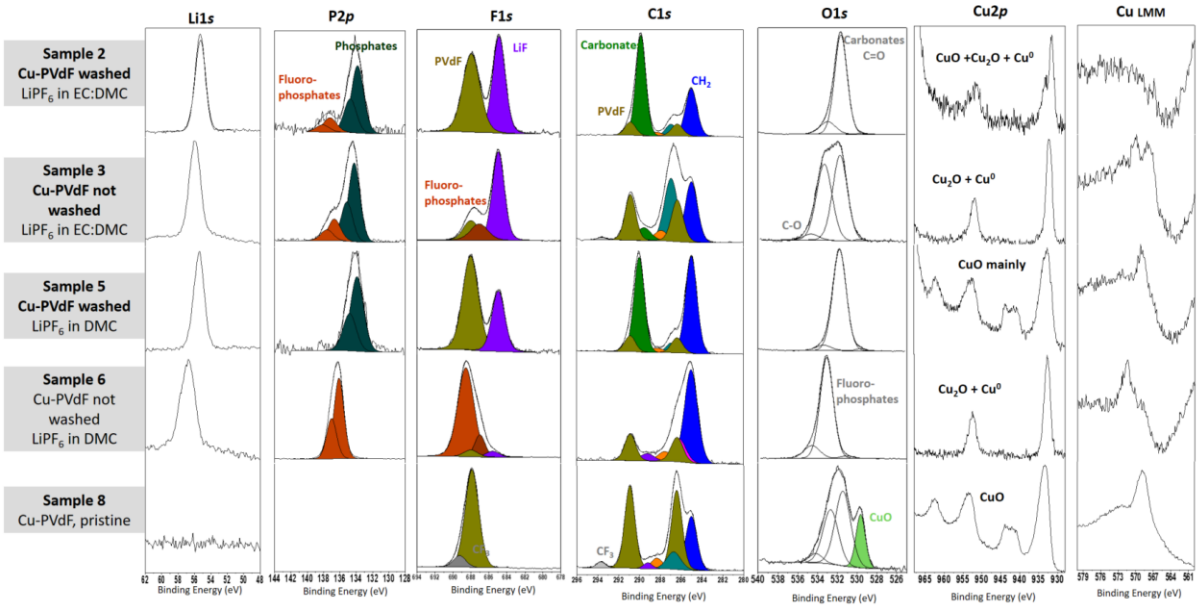


| XPS Quantification | | C | C PVdF | O (Cu) | O | Cu | F PVdF | F LiF | F Fluoro | P Phosph | P Fluoroph | Li |
|---|---|---|---|---|---|---|---|---|---|---|---|---|
| $LiPF_6$ in EC:DMC | Sample 2 washed | 18.4 | 3 | 0.2 | 37.1 | **0.1** | 3.1 | 2.8 | | 0.6 | 0.1 | 34.6 |
| | Sample 3 not washed | 10.9 | 5.6 | 0.1 | 11.8 | **0.3** | 6.2 | 22.2 | 5.9 | 2.5 | 0.8 | 33.8 |
| $LiPF_6$ in DMC | Sample 5 washed | 22.4 | 3.4 | 0.5 | 35.4 | **0.5** | 3.7 | 1.9 | | 0.5 | | 31.8 |
| | Sample 6 not washed | 4.5 | 1.5 | | 22.4 | **0.3** | 1.8 | 1.5 | 32.6 | | 13.6 | 21.8 |
| Pristine | Sample 8 pristine | 20.1 | 32.4 | 1.6 | 6.5 | **2.4** | 36.9 | | | | | |

Supplementary Fig. 5: **XPS of ex-situ copper-PVDF samples** after undergoing intermittent reduction: cycled in 1M $LiPF_6$ in EC:DMC electrolyte and washed with DMC (Sample 2); cycled in 1M $LiPF_6$ in EC:DMC electrolyte without DMC wash (Sample 3); cycled in 1M $LiPF_6$ in DMC electrolyte and washed with DMC (Sample 5); cycled in 1M $LiPF_6$ in DMC electrolyte without DMC wash (Sample 6); stored in 1M $LiPF_6$ in DMC electrolyte without cycling and washed with DMC (Sample 8);

We compare the ex-situ XPS spectra of our post-mortem Cu-PVDF samples (Supplementary Fig. 5) with what is reported in the literature [Dedryvère, R. et al*., J. Phys. Chem. B* **109** (2005)]. On O1*s* level, both $Li_2CO_3$ and alkyl carbonates are characterized by a main peak at 532 eV attributed to COOLi, while alkyl carbonates and LEDC display an additional shoulder at 533.5 eV corresponding to C-O. Our samples display the main peak at 532 eV with only a minute intensity of the 533.5 eV shoulder, indicating that $Li_2CO_3$ is predominant. This is confirmed by the C1s level: the spectra displays a high intensity peak at 289.9 eV attributed to the carbon of the carbonate function (R-O$\underline{C}OO^-$), but only little intensity 286.5 eV attributed to $\underline{C}$-$O^-$. Therefore the carbonate group is primarily comprised of $Li_2CO_3$, for both DMC and EC:DMC electrolyte. While this apparently contradicts the IR observations, such a discrepancy can be explained by aging of the samples between their preparation and the XPS measurement.

Considering the F1*s* level, the fluorophosphates peak disappears after DMC-washing, which effectively removes the remaining $LiPF_6$ salt, confirmed by the evolution of the P2*p* spectrum. The cleaned electrodes show the PVDF binder peak at 687.9 eV, as well as evidencing the formation of LiF (685.0 eV), which could not be identified from IR-FEWS alone, because of the similarity of its only band with that of P-F.

The O1*s* level spectrum (peak at 529.4 eV) reveals the presence of copper oxide in the pristine sample, more precisely identified as CuO considering the spectra of Cu2*p* and Cu Auger levels. After cycling, the O1*s* copper oxide peak is no longer detected, masked by the SEI covering the sample, which is confirmed by the overall decreased intensity of the Cu2*p* peaks (Cu quantified at 2.4% for pristine sample, and below 0.5% for cycled samples). In non-washed samples (3 and 6), these spectra indicate a majority of either $Cu_2O$ or $Cu^0$ (both showing similar Cu2*p* peaks but confirmed by the different Auger features), while CuO is no longer detected, in line with the aforementioned copper oxide reduction. Surprisingly, CuO is still detected in DMC-washed sample 5, whether because $Cu_2O$/Cu was washed away or by later unintentionally reoxidation.

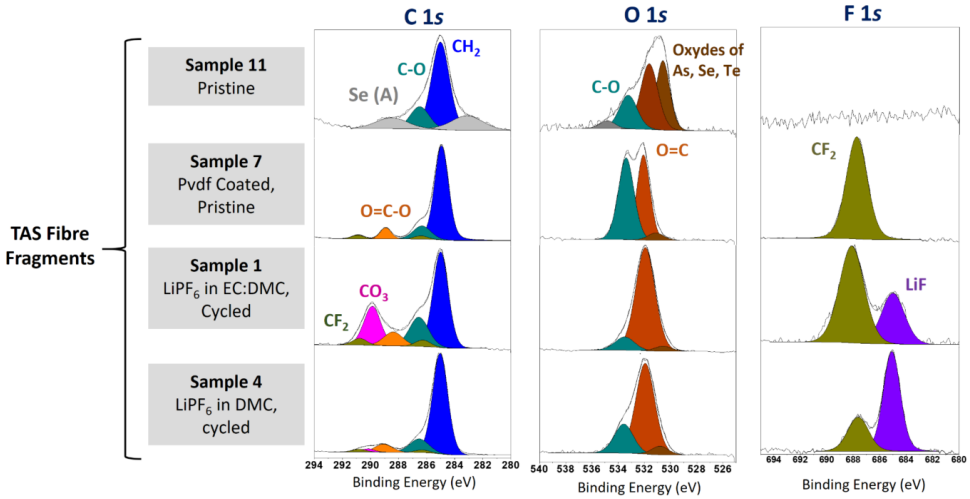


| | C | O | F | Li | As | Te |
|---|---|---|---|---|---|---|
| **Sample 7 - Pristine-PVDF** | 78.1 | 12.8 | 5.8 | 1.3 | 0.1 | 0.9 |
| **Sample 1 - $LiPF_6$ in EC:DMC cycled** | 42.2 | 36 | 1.5 | 14.2 | 0.5 | 1.1 |
| **Sample 4 - $LiPF_6$ in DMC cycled** | 55.6 | 19.5 | 7.4 | 12 | 0.5 | 0.8 |

Supplementary Fig. 6. **XPS of fragments of TAS fibre**. Pristine fibre (Sample 11); pristine fiber embedded in a copper-PVDF electrode and recovered without cell assembly (Sample 7); after undergoing intermittent reduction in 1M $LiPF_6$ in EC:DMC electrolyte and washed with DMC (Sample 1); cycled in 1M $LiPF_6$ in 1M $LiPF_6$ in DMC electrolyte and washed with DMC (Sample 4).

Finally, we measured XPS spectra of fragments of TAS fibre, either pristine (Sample 11), embedded and recovered from the Cu-PVDF slurry (Sample 7), or recovered from a cycled cell (Samples 1 and 4), as shown in Supplementary Fig. 6. Considering the F1*s* level, the samples with PVDF show the expected characteristic peak at 688.8 eV. Strikingly, the cycled samples also show the LiF peak at 685 eV, indicative of SEI deposition on the fibre.

## Supplementary: X-Ray Diffraction (XRD) pristine Cu-Pdvf samples

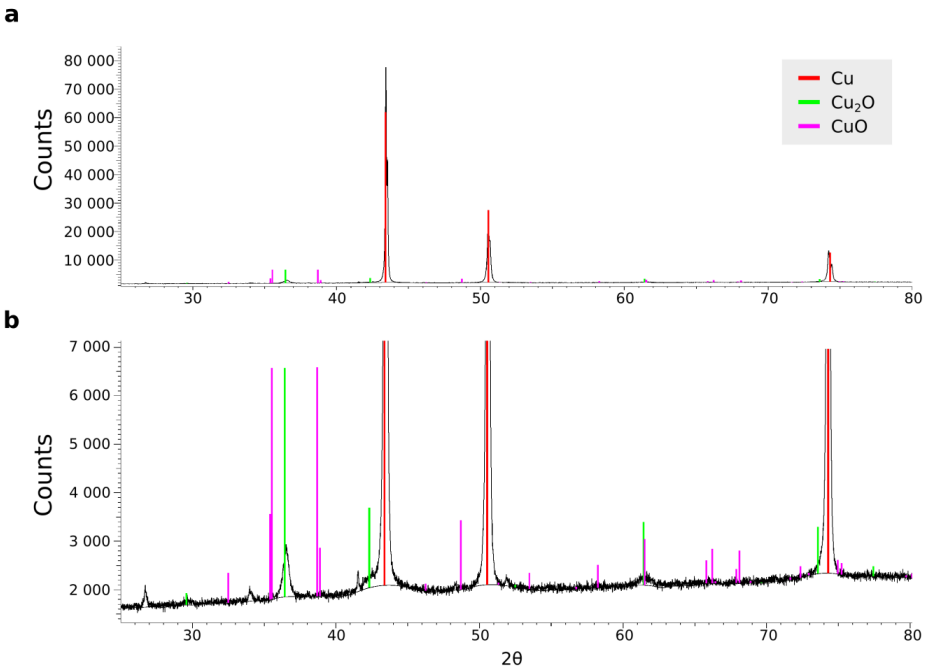


Supplementary Fig. 7. **Powder X-ray diffractogram of pristine copper powder**. **a** Complete diffractogram. **b** Zoom along the y-axis. Reference peaks of metallic copper (red), copper oxide (i) (green) and copper oxide (ii) (pink) are shown.

A X-ray diffractogram of pristine Cu powder is reported in Supplementary Fig. 7. A measurement on an overnight dried Cu-PVDF electrode was also performed, with an identical outcome. Besides the peaks of metallic copper (red) which dominate the diffractogram, low intensity peaks can be attributed to $Cu_2O$ (green), while CuO cannot be detected. This may appear incoherent with XPS observations of Supplementary Fig. 5, which concluded that a majority of CuO is present in the pristine sample, not $Cu_2O$. Such a discrepancy can be reconciled by keeping in mind that XPS solely probes solely 50-100 Å of the Cu particles surfaces (the most oxidized state of Cu (CuO) while XRD probe a deeper part of the particles (less oxidized $Cu_2O$). Likely, both oxides are involved in the process.

## Supplementary: Open circuit voltage of a pristine cell

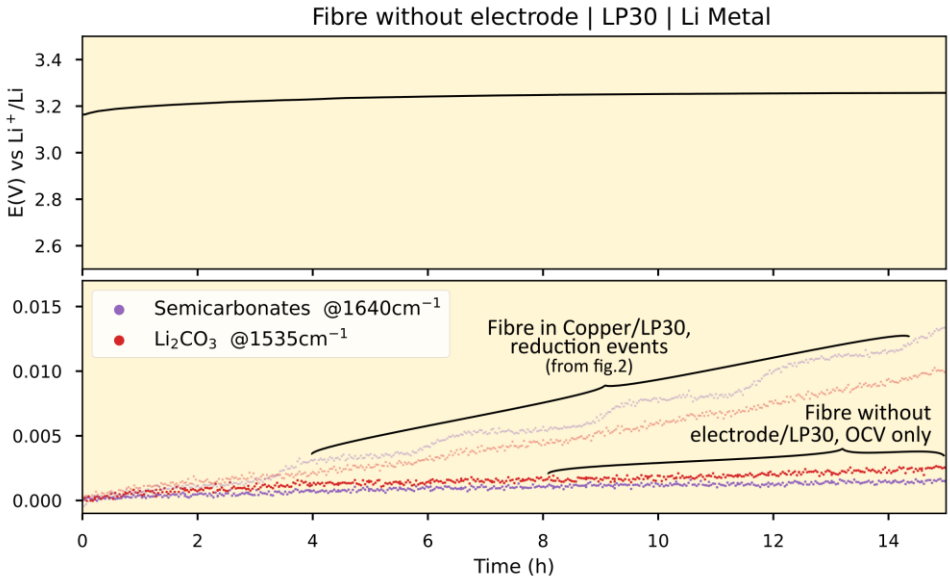


Supplementary Fig. 8. OCV voltage profile (upper panel) of a TAS fibre|LP30|Li metal cell, without active electrode material on; detailed $A(t)$-$A(t_0)$ absorbance variations (lower panel) for two selected wavenumbers representative of $Li_2CO_3$ (1525 $cm^{-1}$, red), and lithium semi-carbonates (1640 $cm^{-1}$, purple). For comparison, we reproduce wavenumber tracking from Figure 2b (shaded).

## Supplementary: Discussing risk of electrochemical rate limitations

Regarding possible risk of electrochemical rate limitations arising from the Li-metal counter electrode surface: while the Li-metal counter electrode surface will certainly have its own interfacial impedance that could control the impact electrochemical reduction step, this does not appear to be the case with this cell configuration and reduction protocol. The drop-cast working electrodes are paired with Li metal disks, giving rise to larger surface area for Li-metal than the working-material under investigation. Galvanostatic pulses ensure electron transfer through the working electrode of interest when currents are positive allowing, thus giving continuity between samples. We acknowledge that this may also drive spatial inhomogeneities that are yet to be well understood and may be, in part, a source for the differences observed herein. Nevertheless, this work establishes the viability and prospects for SEI characterization with IR-FEWS and future experiments can be designed to systematically understand how the choice of cathode material and electrochemical conditions (i.e. galvanostatic or potentiostatic) jointly impact the chemical composition and functionality of the SEI on the anode surface.

## Supplementary: Detailed MCR-ALS - LP30 reduction on copper powder

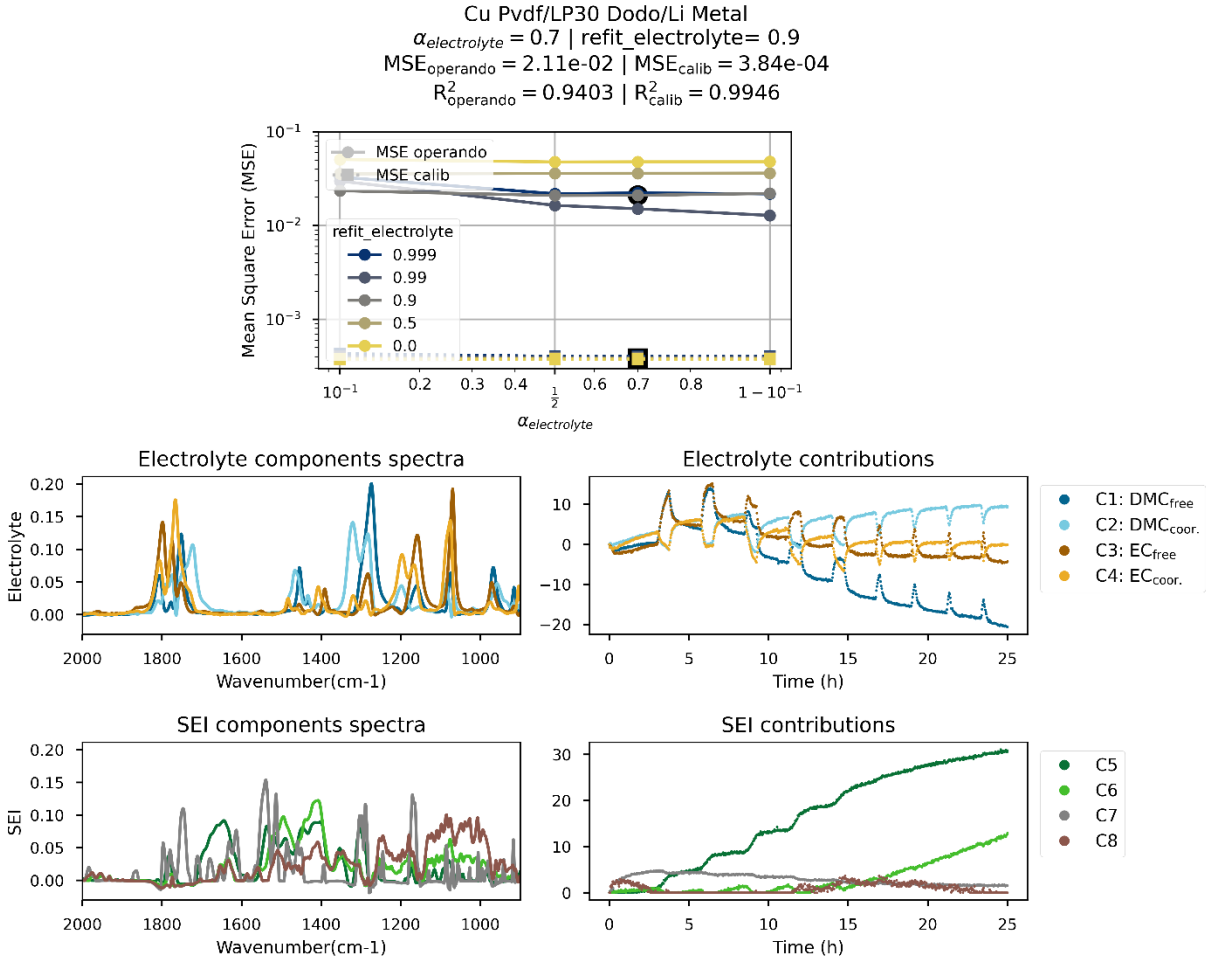


Supplementary Fig. 9. **Detailed MCR-ALS for the Cu-PVDF | LP30 | Li cell.** MSE of operando and calibration spectra (solid and dashed lines, respectively), for several values of $\alpha_{electrolyte}$ and electrolyte refitting parameter (upper panel). The decomposition reported in the main text is highlighted with black markers, and detailed on the four lower panels: spectra (left panels) and associated contributions (right panels) for electrolyte (middle panels) and SEI components (lower panels).

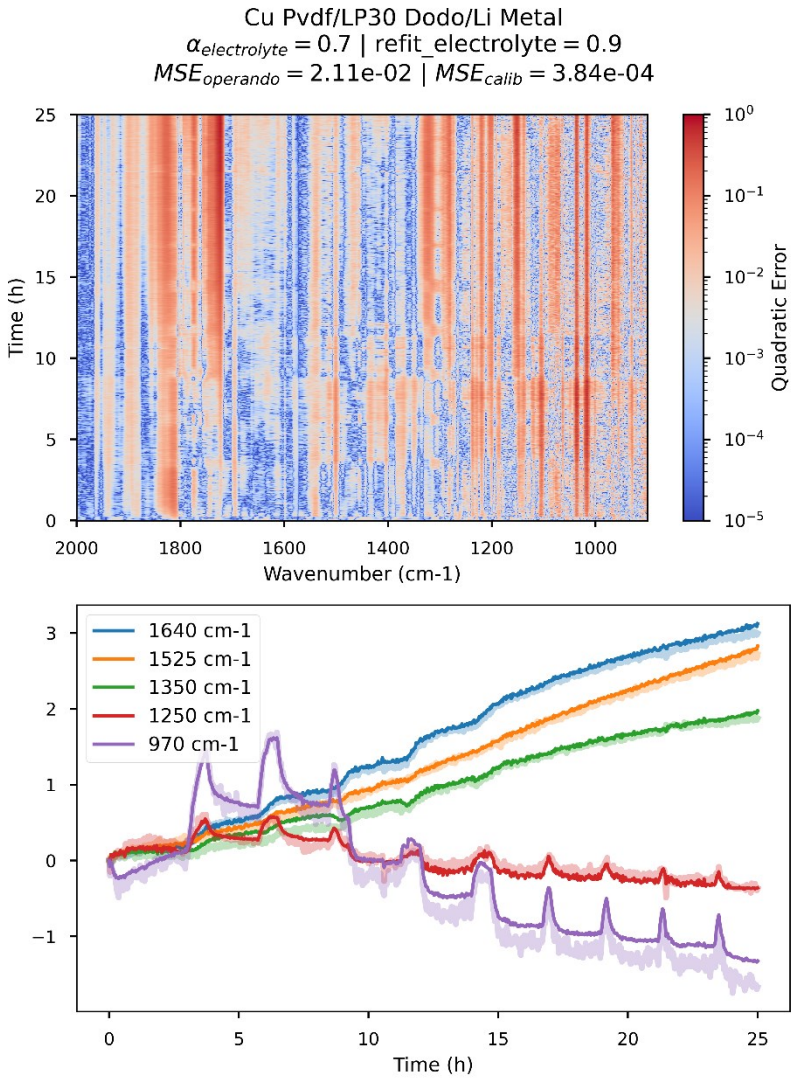


120

121 Supplementary Fig. 10. **Detailed MCR-ALS for the Cu-PVDF | LP30 | Li cell.** Quadratic error between operando data D and
122 reconstructed from MCR-ALS ($CS^T$) (upper panel). Comparison of operando data D (transparent lines) and reconstructed data
123 from MCR-ALS ($CS^T$) (solid lines) at selected wavenumbers.

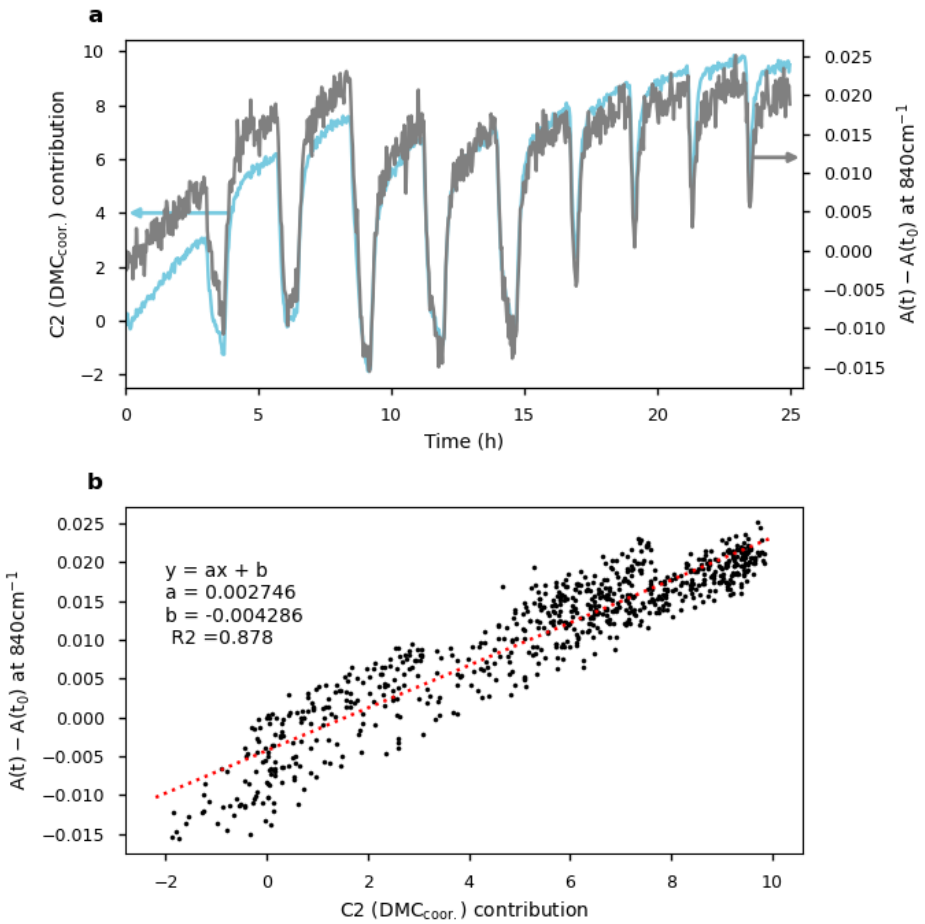


Supplementary Fig. 11. Copper-PVDF|LP30|Li Metal cell: **a**, contribution of the second MCR-ALS electrolyte component, attributed to $Li^+$-coordinating DMC (left axis, light blue), $A(t)$-$A(t_0)$ variation of the $PF_6^-$ band tracked at 840 $cm^{-1}$ (right axis, grey). Both variable show similar variations: $Li^+$ coordination effect matches anion absorbance variations. **b**, Correlation between C2 ($Li^+$-coordinating DMC component) and absorbance at 840 $cm^{-1}$. A linear regression shows as red-dotted line.

## Supplementary: Rank Analysis & Principal Component Analysis - LP30 reduction on copper powder

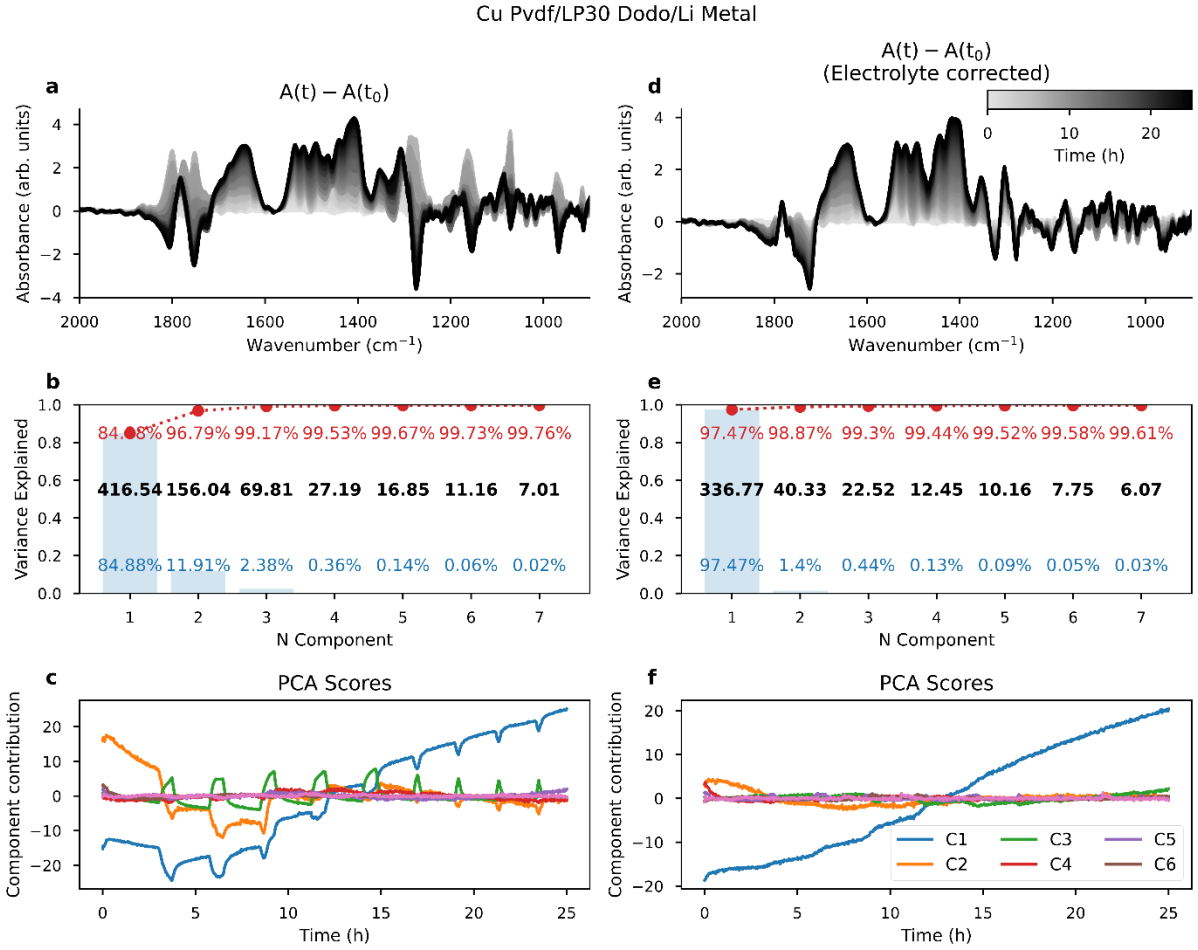


Supplementary Fig. 12. **Discussing the choice of number of components for the SEI.**

The choice of number of components for MCR-ALS was guided by a chemical rank analysis as well as trial-and-error testing.

The many wavenumbers making the spectroscopic data do not evolve independently, but are linearly related. Typically, two consecutive data points belonging to the same vibrational band show very similar evolution. Linear factorization techniques like MCR-ALS extract these variations. It should be discussed how many components are actually needed to describe these evolutions; in the linear algebra formalism, this means determining the rank of the data matrix $D$, in other words, the number of species showing linearly distinct evolution. In the case of experimental data, the presence of noise or other unlinearities (imperfect background fitting, …) may also increase the mathematical rank, which is why a chemical rank must be considered.

As standardly practiced[26] [Meloun et al. *Analytica Chimica Acta (2000)*], and shown in Supplementary Fig. 12, Principal Components Analysis (PCA) was applied to the experimental data shown in **a**. The orthogonal spectra components are represented in panel **b** by their singular value (black text), contribution to variance (blue bar plot) and cumulative variance explained (red dashed line). Their respective contributions score over time are shown in **c**. Hence, depending on the variance explained threshold targeted, three to five components may be necessary to reconstruct the original data.

However, in the case of our data, we heavily constrain four components to the spectra to the original electrolyte calibration of Figure 1. As a result, more components will be necessary. To determined how

many, we fitted and subtracted the electrolyte components to the operando data by Ordinary Least Square (OLS) regression, providing an approximated electrolyte contribution decoupled from SEI. The resulting data (Supplementary Fig. 12d) was similarly subjected to PCA, which results shows in subfigures e and f. Strikingly, on its own, the first component encapsulates 97.6% of the variability (blue in Supplementary Fig. 12e), showing that all SEI species are growing at quite similar rates. Additional smaller contributions components remains necessary to accurately model finer variations.

While PCA provides an estimation of the chemical rank, it should be noted that could not be directly translated to MCR-ALS component number. Firstly, PCA is systematically applied on mean-subtracted data, which was not the case in the MCR-ALS pipeline. Secondly, PCA spectral loadings are allowed to be negative, while we constrained MCR-ALS SEI components to positivity, hence requiring more components to achieve similar MSE. Finally, the constraint refitting and subtracting electrolyte from SEI component, which allows better electrolyte/SEI decoupling, was found to also increase the MSE compared to PCA, meaning a more interpretable decomposition comes at a cost of less accuracy in fitting the data.

For these reasons, the number of components was ultimately chosen by trial-and-error method, considering mean square error and interpretability of the spectra.

**Supplementary: Washing the electrodes to evidence SEI**

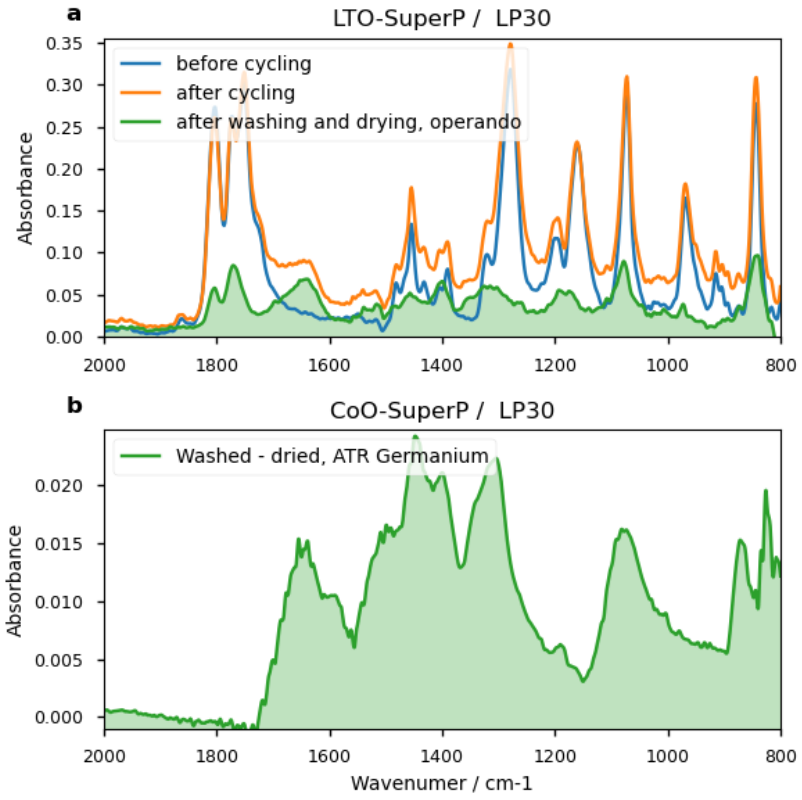


Supplementary Fig. 13. **Ex-Situ post-mortem FTIR spectra of electrode materials**. **a**, LTO/SuperP electrode cycled in LP30 against Li metal in the TAS fibre operando cell: initial spectrum (blue); spectrum after cycling notably showing the semi-carbonate band at 1640 $cm^{-1}$ (orange); spectrum acquired after opening the cell, repeatedly rinsing the electrode with DMC and subsequent drying, EC bands appear with diminished intensity, while semi-carbonate band remains of a similar amplitude (green) **b**, CoO/SuperP electrode cycled in LP30 against Li metal, recovered, washed with DMC and dried under vacuum, and finally tested by ATR-FTIR (Ge crystal).

**Supplementary: Testing SEI Salt Solubility**

We used commercial $Li_2CO_3$. LMC and LEDC were synthesised by ourselves. Lithium ethylene monocarbonate, ($HOCH_2CH_2OCOOLi$, or LEMC) was also prepared, as it was recently discussed to be a potential SEI component instead of LEDC [Wang et al. *Nat. Chem.* (2019)], even though additional evidence would be necessary to fully confirm this hypothesis.

Preparation of LMC (inspired by [Wang et al. *Nat. Chem.* (2019)]):

To a Schlenk flask of magnetically-stirred anhydrous methanol (20 mL at 0°C) was added 1.6M nBuLi/hex (16 mL, 25.6 mmol), dropwise. The reaction was let warm at room temperature (20°C-25°C) and stirred for 30 minutes. Afterwards, $CO_2$ was bubbled in the stirred reactional media for 2 hours, after which the remaining solvent was evaporated under vaccum, providing a white solid successively washed with dry acetonitril and dry diethyl ether, and dried under vaccum for at least 12 hours. It was obtained 1.65g of LMC (20.2 mmol, 79% yield).

Preparation of LEMC (inspired by [Wang et al. *Nat. Chem.* (2019)]):

To a Schlenk flask of magnetically-stirred anhydrous ethylene glycol (8 mL at 0°C) was added 1.6M nBuLi/hex (10 mL, 16 mmol), dropwise. The reaction was let warm at room temperature (20°C-25°C) and stirred for 30 minutes. Afterwards, $CO_2$ was bubbled in the stirred reactional media for 3 hours, during which time hexane phase evaporated. Dry pyridine (20mL) was added to the flask which was left resting for 48 hours, during which time a solid deposit formed on the walls of the flask. The solid was recovered and successively washed with anhydrous acetonitril and anhydrous diethyl ether, and dried under vaccum for at least 12 hours. It was obtained 1.05 g of LMC (9.37 mmol, 59% yield).

Preparation of LEDC [Zhuang et al. *J. Phys. Chem. B* (2005)] :

To a Schlenk flask of magnetically-stirred 1.6M nBuLi/hex (10 mL, 16 mmol) in anydrous diethylether was added 366 mg (5.9 mmol) of anhydrous ethylene glycol, dropwise, at 0°C. The reaction was let warm at room temperature (20°C-25°C) and stirred for 30 minutes. Afterwards, $CO_2$ was bubbled in the stirred reactional media for 2 hours, until complete solvent evaporation. A white solid was recoverd, succesively washed with anhydrous acetonitril and anhydrous diethyl ether, and dried under vaccum for at least 12 hours.

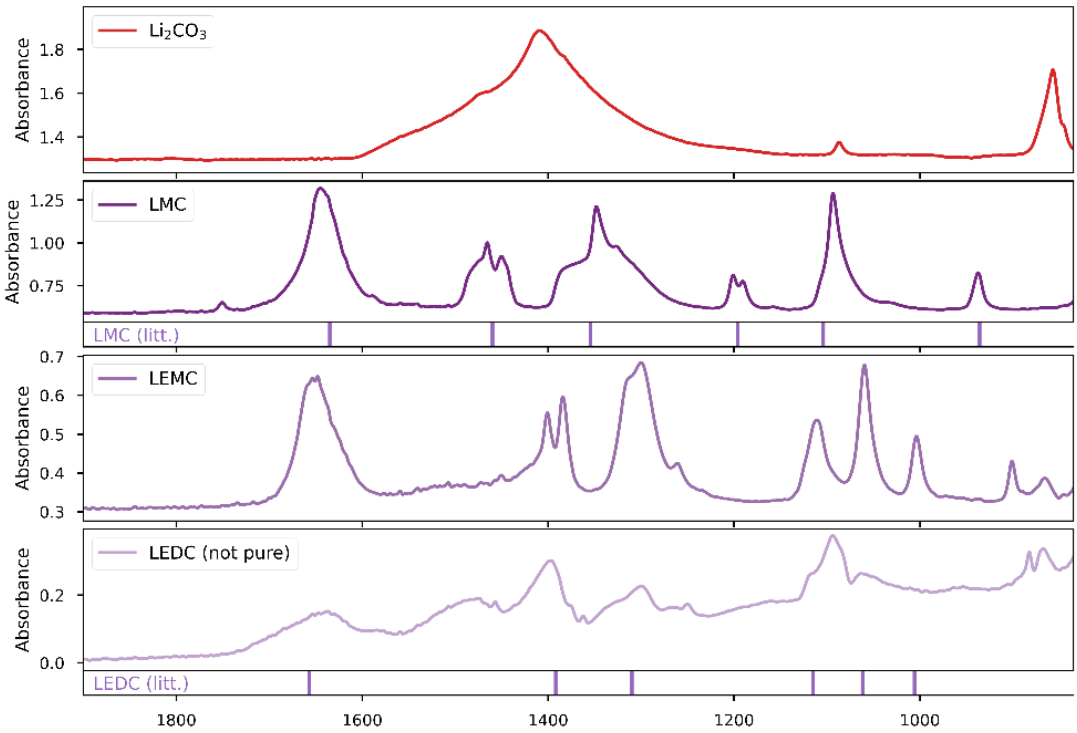


Supplementary Fig. 14. **a** ATR-FTIR (diamond) spectra of four lithium salts possibly present in the SEI: $Li_2CO_3$ (commercial), lithium methyl carbonate (LMC, synthesized by ourselves), lithium ethyl mono-carbonate (OH-$CH_2$-$CH_2$-OCOOLi, or LEMC, synthesized by ourselves) and lithium ethyl dicarbonate (LEDC, synthesized by ourselves, not pure).

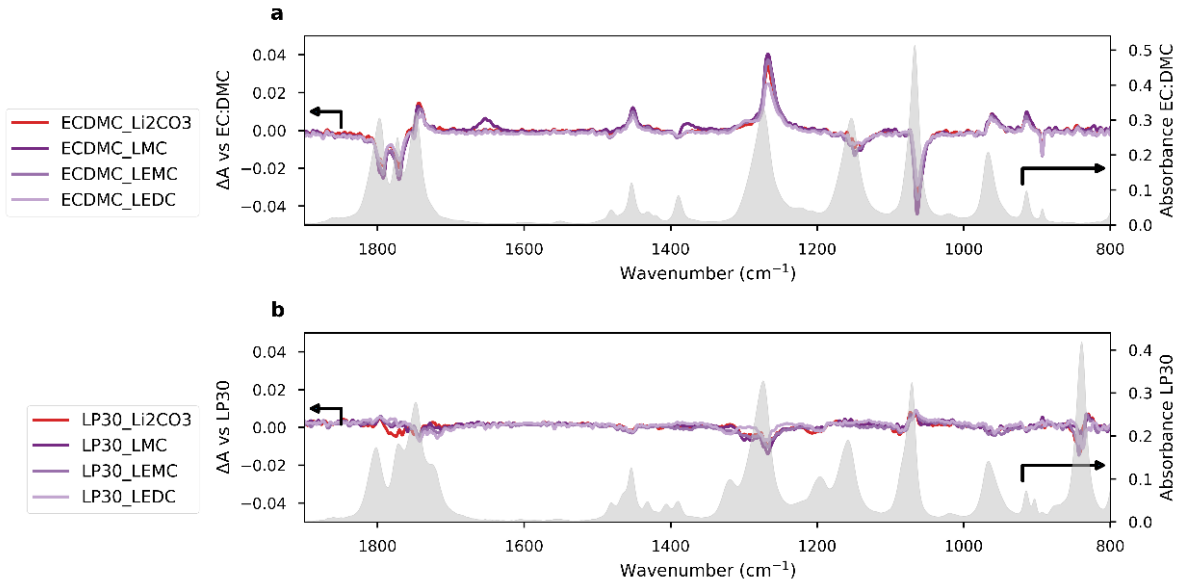


Supplementary Fig. 15. **a** ATR-FTIR spectrum of EC:DMC (1:1 w:w) solvent (grey, right axis) and difference spectra from subtracting EC:DMC spectrum to spectra of saturated solution of $Li_2CO_3$ , LMC, LEMC, LEDC in EC:DMC (left axis). **b** ATR-FTIR infrared spectrum of LP30 electrolyte (grey, right axis) and difference spectra from subtracting LP30 spectrum to spectra of saturated solution of $Li_2CO_3$, LMC, LEMC, LEDC in LP30 (left axis).

## Supplementary: Discussing the electrochemical stability of TAS glass

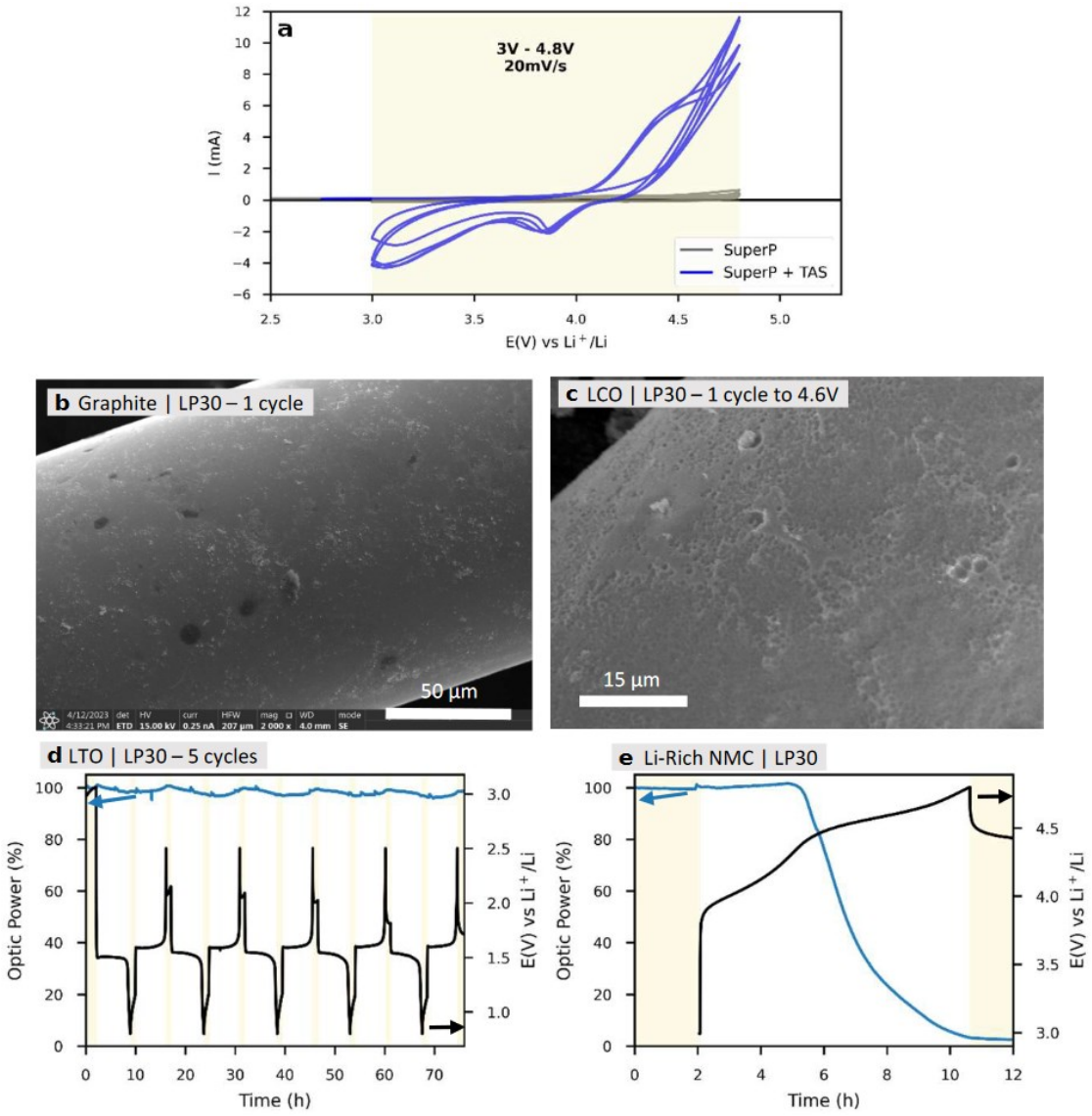


Supplementary Fig. 16. **Electrochemical stability of TAS fibre. a** CV of TAS:SuperP powder mix (blue curve) and SuperP powder (grey curve) between 3V and 4.8V. **b** Ex-situ SEM image of a TAS fibre cycled to 0 V in the electrode of a graphite|LP30|Li cell; **c,** of a TAS fibre after 1 cycle in a LCO|LP30|Li cell, with 4.6V cut-off potential. **d** Evolution of the optic power transmitted through the fibre compared to initial value (left axis, blue) and cell potential (right axis, black) during 'long-cycling' operando experiment of LTO|LP30|Li cell; **e** same with a Li-Rich NMC|LP30|Li cell.

To assess the electrochemical stability of TAS glass, fragments of fibre were ground with conductive carbon SuperP (ratio 9:1 w/w) to increase both the surface area and the contact between the fibre and the carbon and therefore its reactivity, and assembled into 10 mg-loaded LP30 half-cells. Half-cells loaded with 1mg of SuperP were equally prepared as reference. When cycling over the 0-2V range, similar long-term cycling curves were observed comparing the TAS-containing carbon electrode and the TAS-free carbon electrode. This was confirmed by the SEM picture of a TAS fibre that has been cycled to 0 V, which general smoothness was preserved as shown in Supplementary Fig. 16b.

In contrast, a minor oxidative current onset is seen at 4.2 V and then increases strongly (blue curve in Supplementary Fig. 16a) upon further increasing the oxidation current. Under the same conditions, the TAS-free cell barely shows any oxidation current. This is indicative of degradation of the TAS fibre at high voltage (>4.3 V) and is further confirmed by the corrosion pits observed on the SEM picture of

a fibre cycled to 4.6 V (Supplementary Fig. 16a). Noteworthy, the reductive current between 3V and 4V is attributed to subsequent reduction of the primarily oxidized species and was not observed when limiting the scan to 4V.

To further confirm this range of stability in operando conditions, we compare the LTO/LP30/Li metal cell of Figure 7 with a Li-rich-NMC/LP30/Li metal cell, having the TAS fibre in the LTO and Li-rich NMC electrode, respectively. Note the constancy of the optic power guided through the fibre upon cycling for the LTO-based cell, while the optical power drastically drops for the Li-rich NMC cell at a voltage of nearly 4.3V, coinciding with the onset of the oxidation current observed by cyclic-voltammetry measurements. For sake of completeness, we should emphasize that the overall stability window (0-4.3V) may slightly change depending upon the electrolytes used.

## Supplementary: MCR-ALS of Cu-Pdvf samples with varying electrolyte

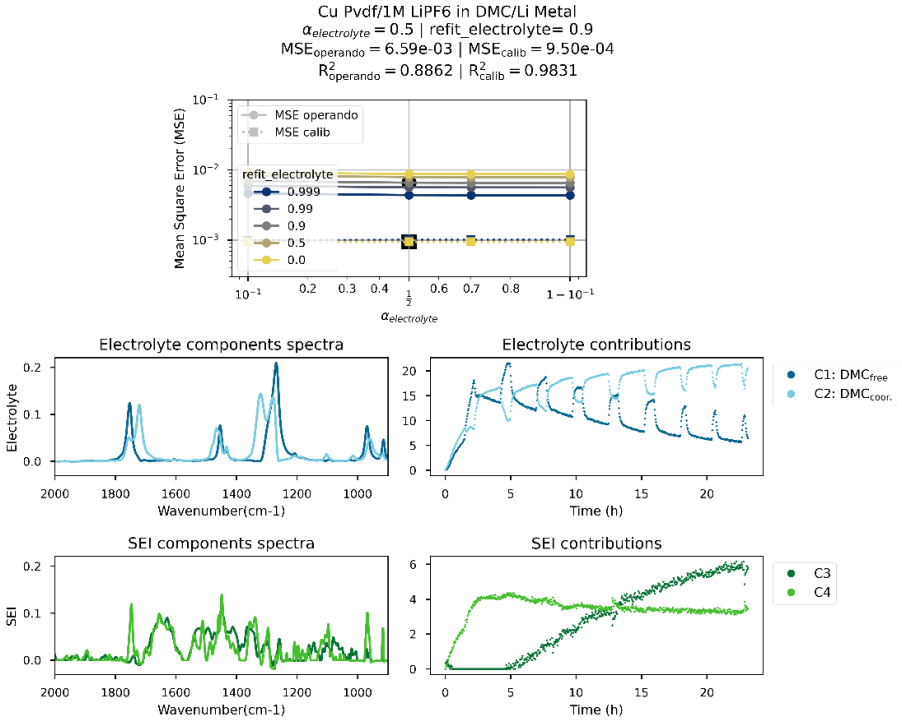


Supplementary Fig. 17. **Detailed MCR-ALS for the Cu-PVDF | 1M $LiPF_6$ in DMC | Li cell.** MSE of operando and calibration spectra (solid and dashed lines, respectively), for several values of $\alpha_{electrolyte}$ and electrolyte refitting parameter (upper panel). The decomposition reported in the main text is highlighted with black markers, and detailed on the four lower panels: spectra (left panels) and associated contributions (right panels) for electrolyte (middle panels) and SEI components (lower panels).

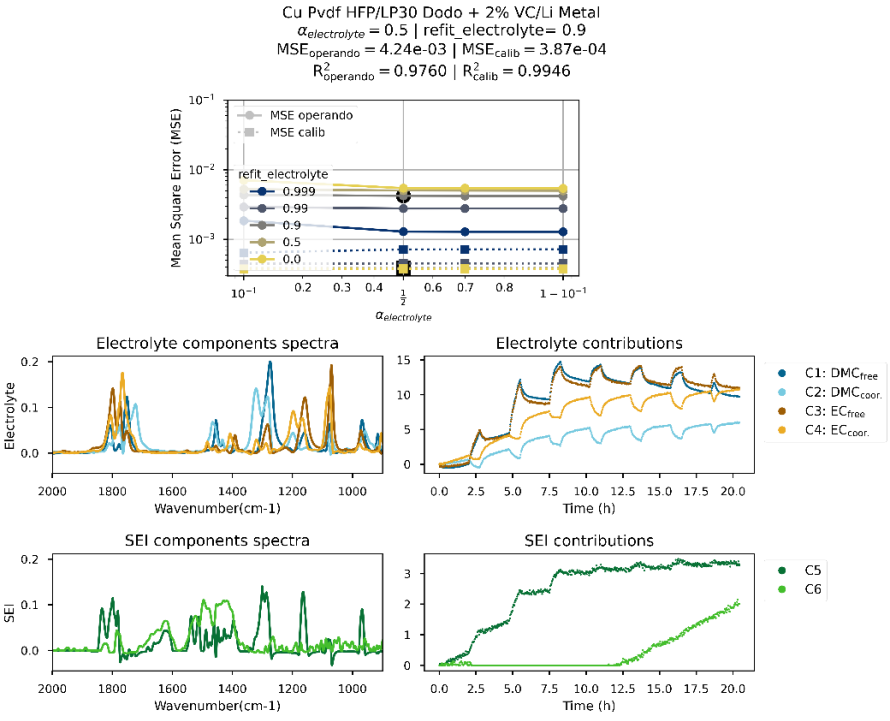


Supplementary Fig. 18. **Detailed MCR-ALS for the Cu-PVDF | LP30+2%VC | Li cell.** MSE of operando and calibration spectra (solid and dashed lines, respectively), for several values of $\alpha_{electrolyte}$ and electrolyte refitting parameter (upper panel). The decomposition reported in the main text is highlighted with black markers, and detailed on the four lower panels: spectra (left panels) and associated contributions (right panels) for electrolyte (middle panels) and SEI components (lower panels).

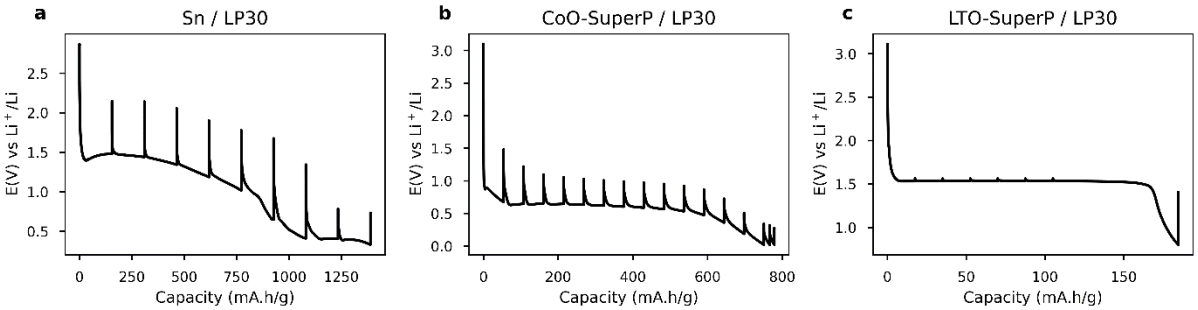


Supplementary Fig. 19. Reduction specific capacity for the three electrode materials: **a,** Sn; **b,** CoO/SuperP; **c,** LTO/SuperP.

**Supplementary - Commercial Electrolyte reduction on various electrode material**

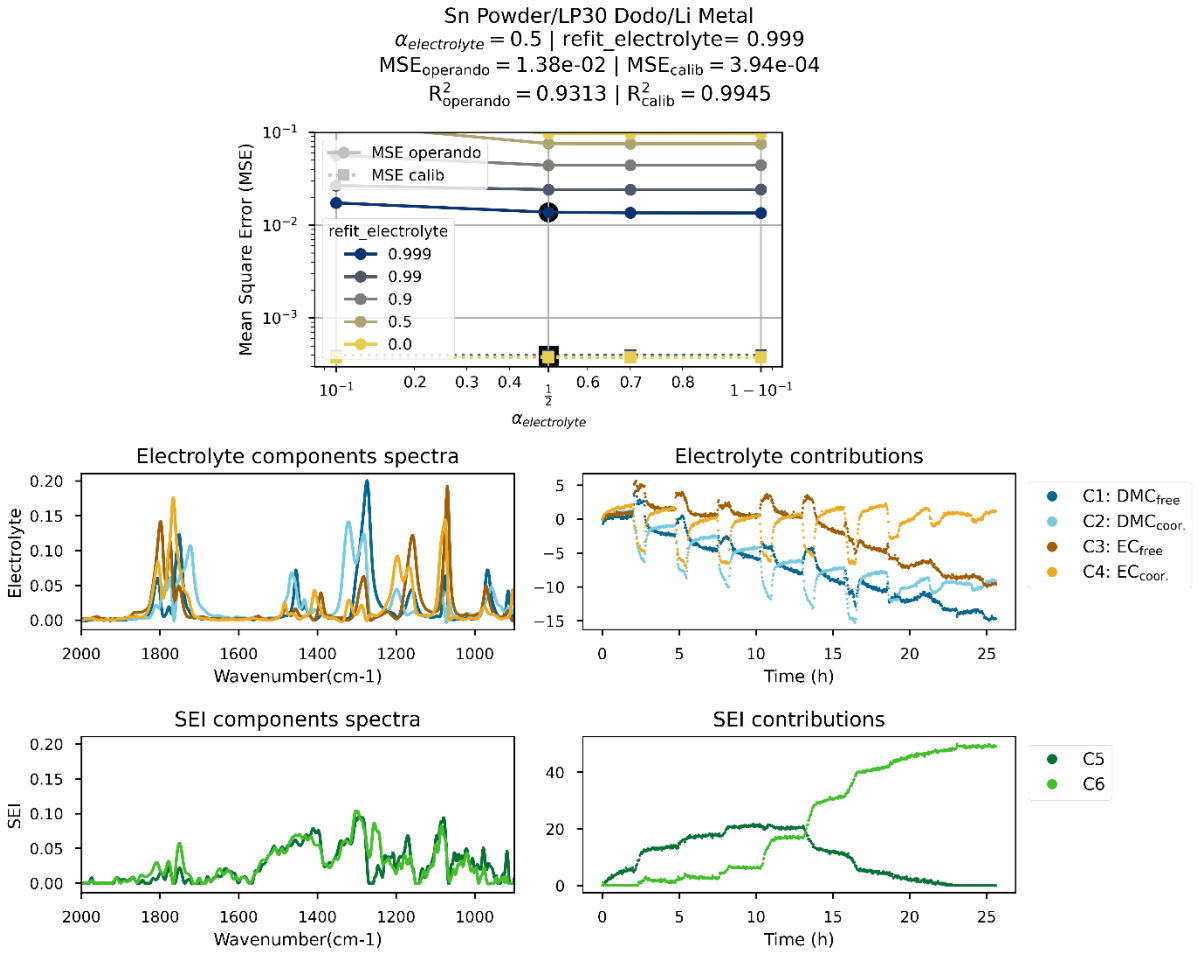


Supplementary Fig. 20. **Detailed MCR-ALS for the Sn | LP30 | Li cell.** MSE of operando and calibration spectra (solid and dashed lines, respectively), for several values of $\alpha_{electrolyte}$ and electrolyte refitting parameter (upper panel). The decomposition reported in the main text is highlighted with black markers, and detailed on the four lower panels: spectra (left panels) and associated contributions (right panels) for electrolyte (middle panels) and SEI components (lower panels).

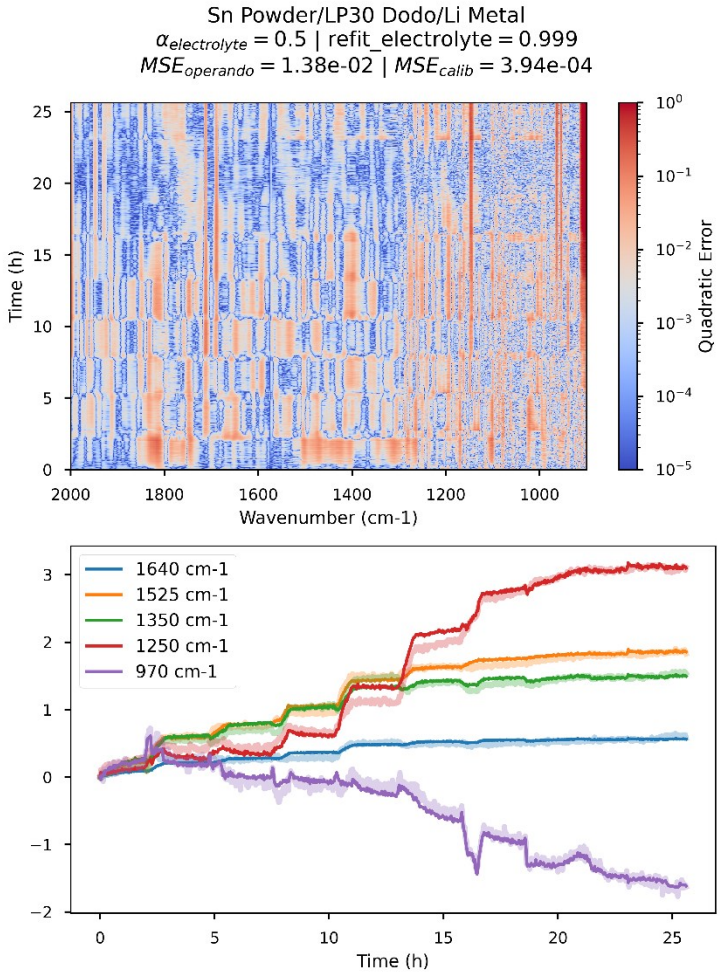


Supplementary Fig. 21. **Detailed MCR-ALS for the Sn | LP30 | Li cell.** Quadratic error between operando data D and reconstructed from MCR-ALS ($CS^T$) (upper panel). Comparison of operando data D (transparent lines) and reconstructed data from MCR-ALS ($CS^T$) (solid lines) at selected wavenumbers.

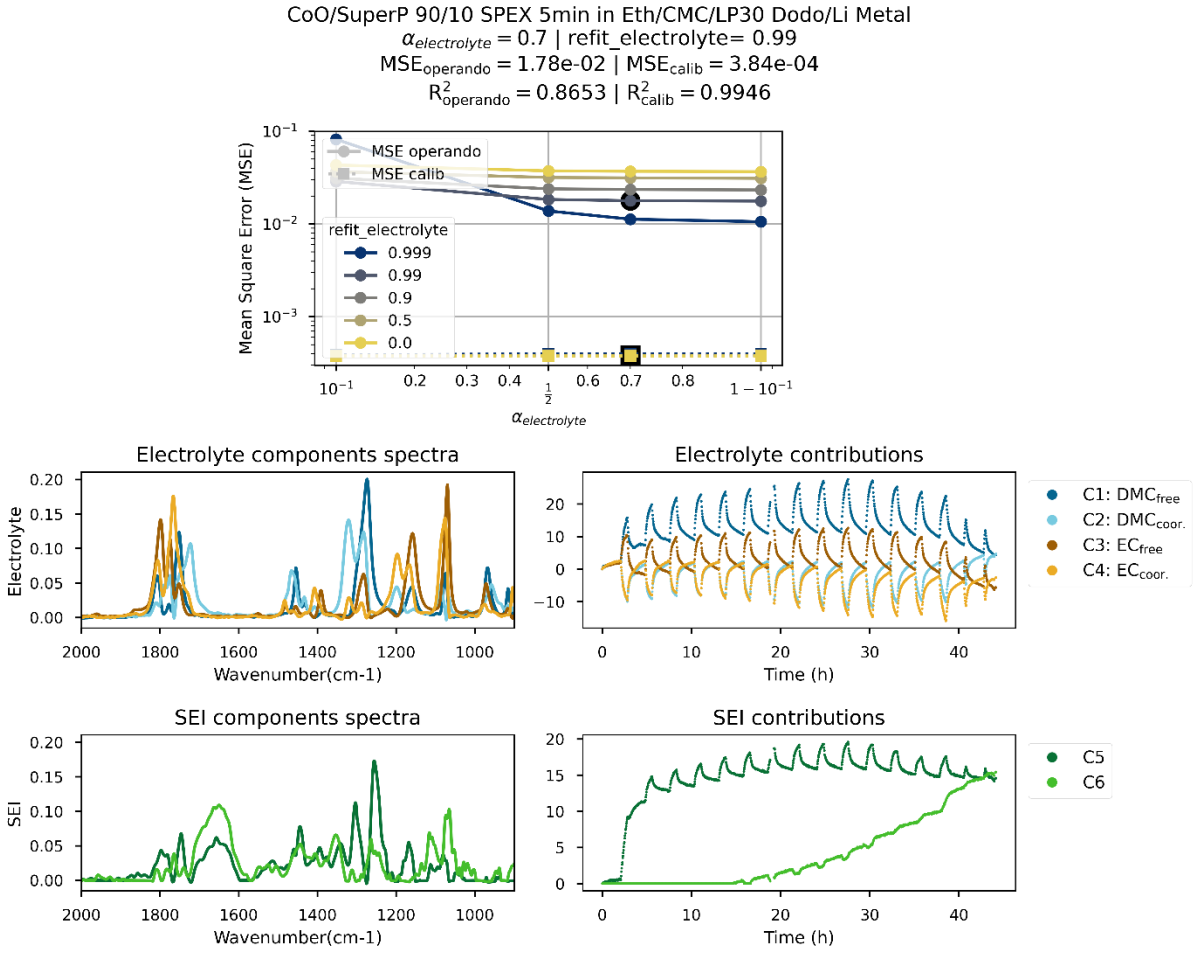


Supplementary Fig. 22. **Detailed MCR-ALS for the CoO/SuperP | LP30 | Li cell.** MSE of operando and calibration spectra (solid and dashed lines, respectively), for several values of $\alpha_{electrolyte}$ and electrolyte refitting parameter (upper panel). The decomposition reported in the main text is highlighted with black markers, and detailed on the four lower panels: spectra (left panels) and associated contributions (right panels) for electrolyte (middle panels) and SEI components (lower panels).

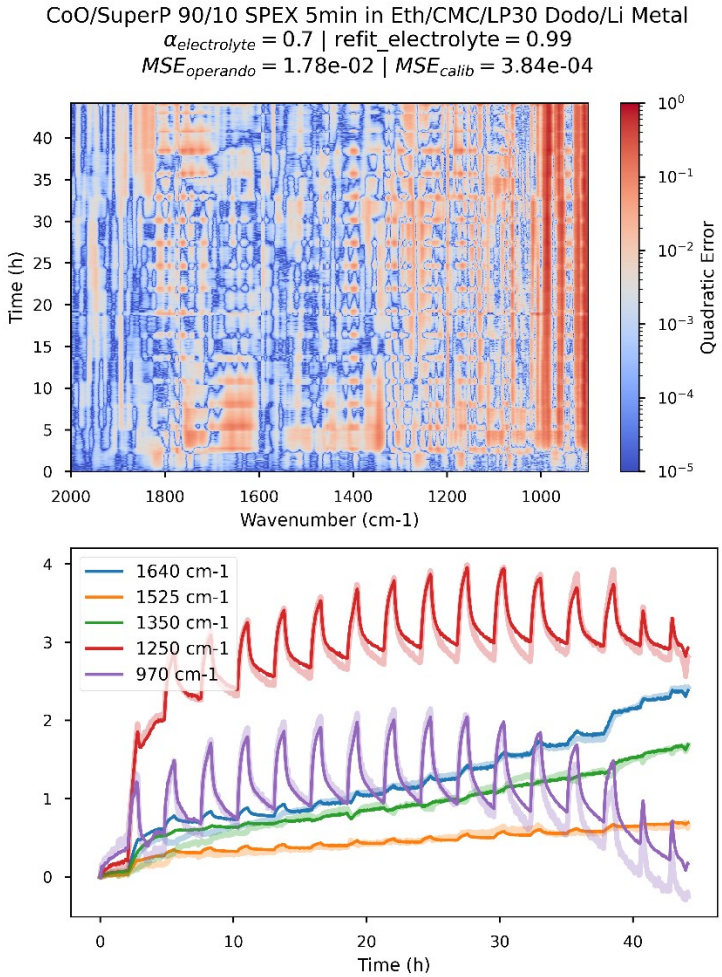


271

272 Supplementary Fig. 23. **Detailed MCR-ALS for the CoO/SuperP | LP30 | Li cell.** Quadratic error between operando data D
273 and reconstructed from MCR-ALS ($CS^T$) (upper panel). Comparison of operando data D (transparent lines) and reconstructed
274 data from MCR-ALS ($CS^T$) (solid lines) at selected wavenumbers.

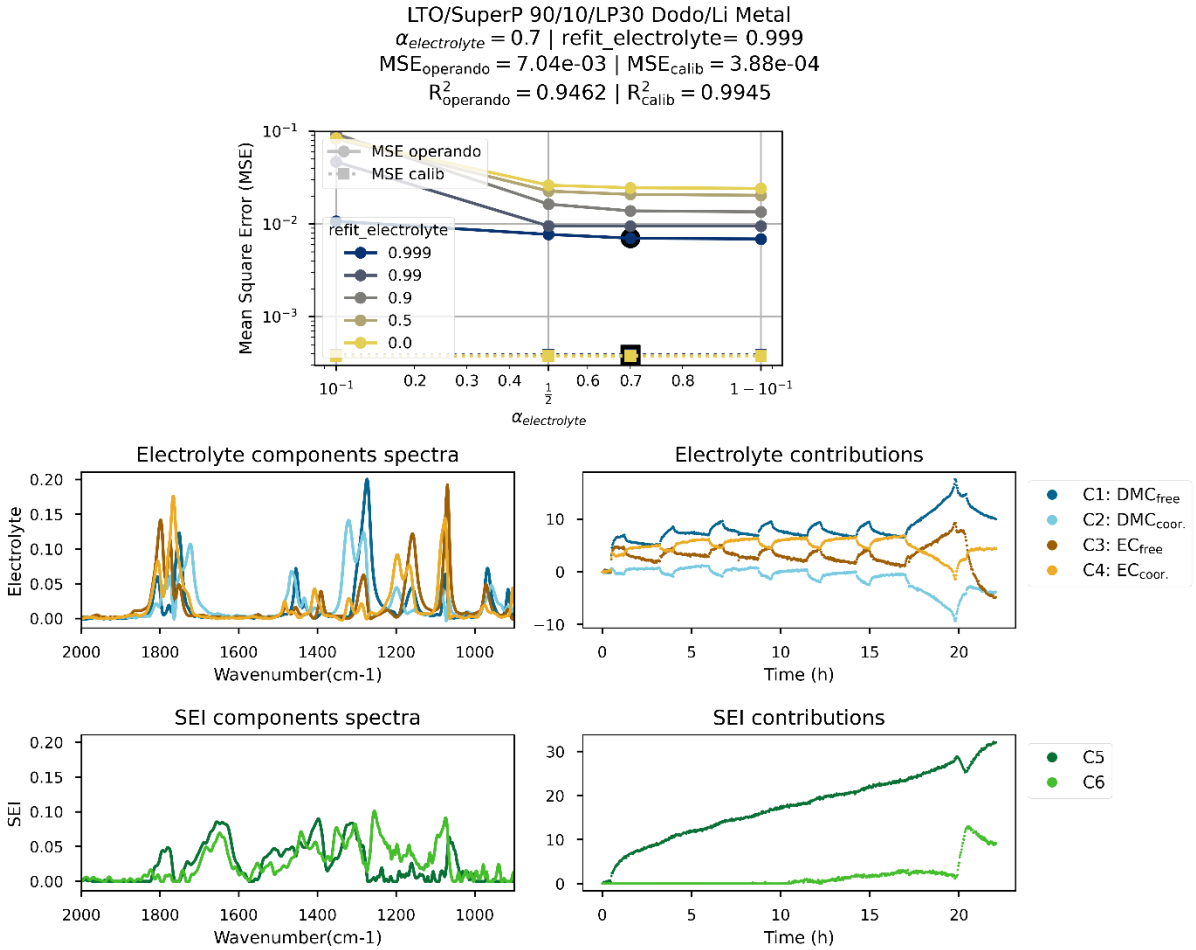


Supplementary Fig. 24. **Detailed MCR-ALS for the LTO/SuperP | LP30 | Li cell.** MSE of operando and calibration spectra (solid and dashed lines, respectively), for several values of $\alpha_{electrolyte}$ and electrolyte refitting parameter (upper panel). The decomposition reported in the main text is highlighted with black markers, and detailed on the four lower panels: spectra (left panels) and associated contributions (right panels) for electrolyte (middle panels) and SEI components (lower panels).

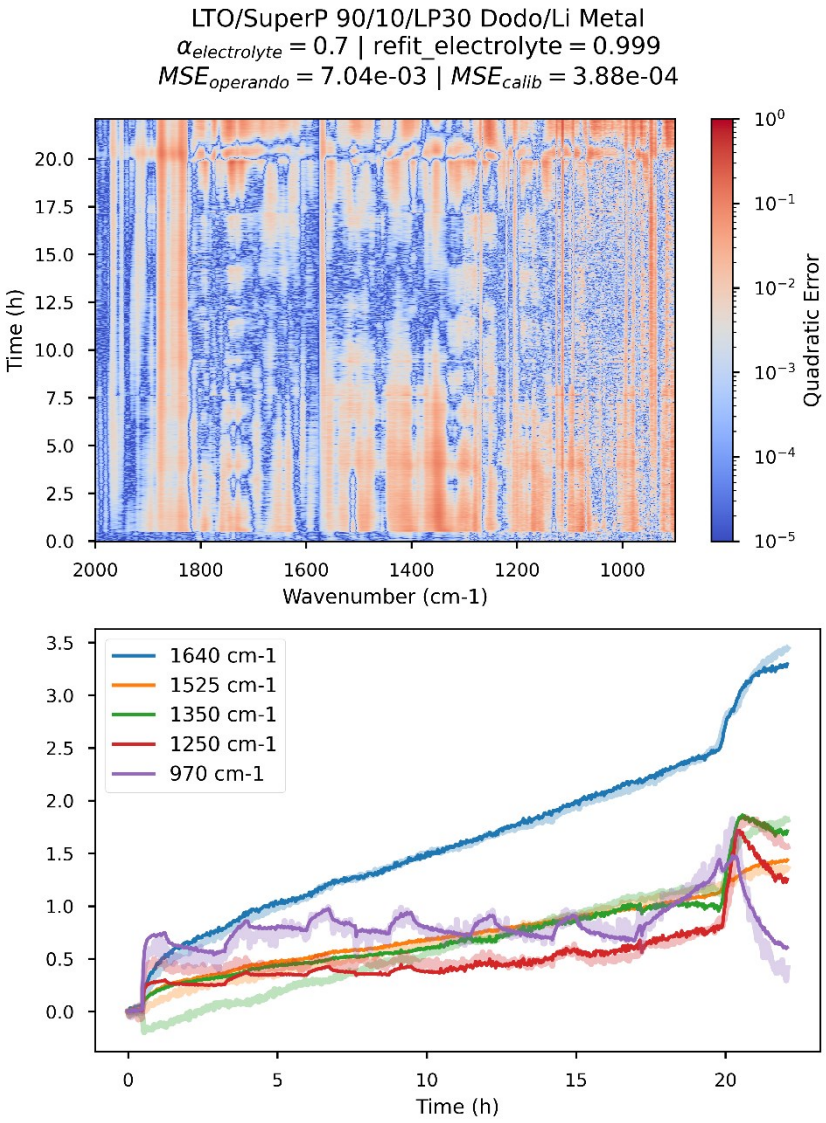


Supplementary Fig. 25. **Detailed MCR-ALS for the LTO/SuperP | LP30 | Li cell.** Quadratic error between operando data D and reconstructed from MCR-ALS ($CS^T$) (upper panel). Comparison of operando data D (transparent lines) and reconstructed data from MCR-ALS ($CS^T$) (solid lines) at selected wavenumbers.

**Supplementary - Commercial electrolyte reduction on LTO – 4000-2600cm$^{-1}$ range**

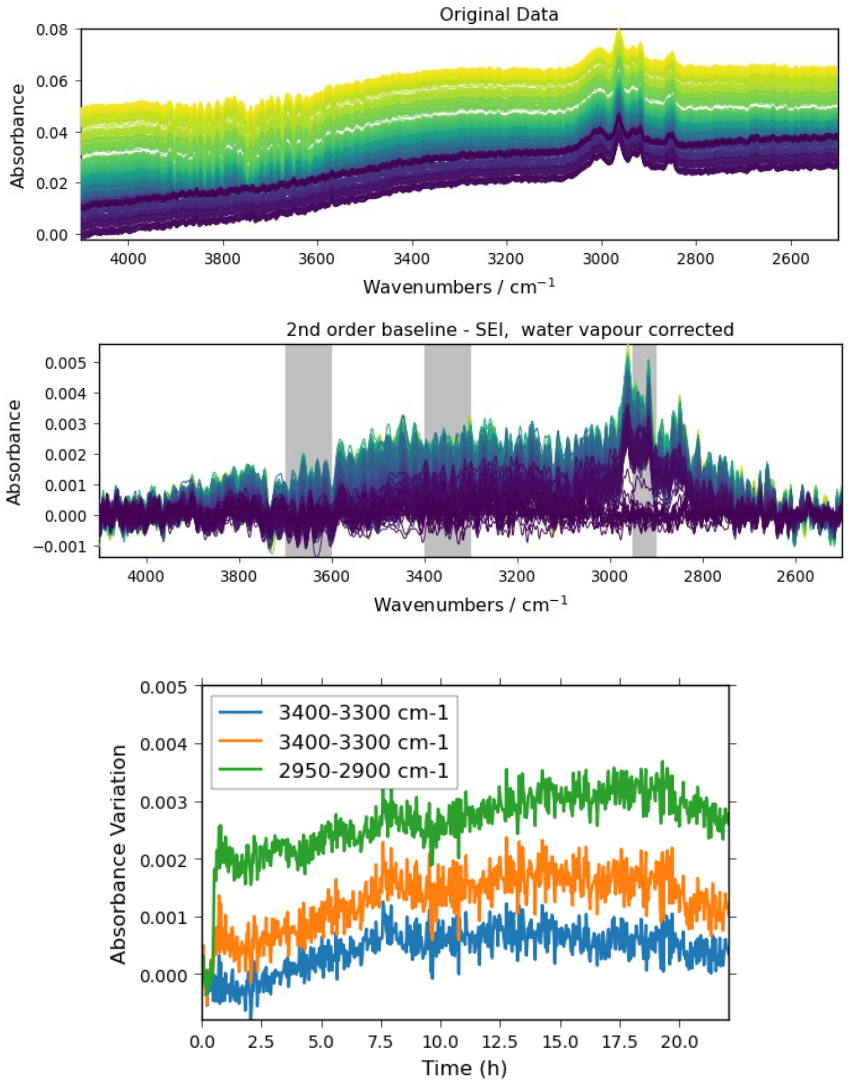


Supplementary Fig. 26. Focus on the 4000-2500 cm$^{-1}$ region for reduction in LTO half-cell: **upper panel**, Absorbance spectra (original data), as acquired by the spectrometer; **middle panel**, $A(t)$-$A(t_0)$, corrected for water vapour and baseline (2$^{nd}$ order polynomial fitted in the 4100-3950 cm$^{-1}$ and 2600-2500 cm$^{-1}$ regions); **lower panel**, temporal evolution in three averaged wavenumber ranges (blue ,3700-3600 cm$^{-1}$;orange, 3400-3300 cm$^{-1}$; green, 2950-2900 cm$^{-1}$). The absorbance in the 3400-3300 cm$^{-1}$ range, corresponding to the maximum of –OH band of LEMC do not show any distinct evolution compared to the other ranges. Hence, the –OH band characteristic of LEMC is not detectable.

The identification of the semi-carbonate presented relies on reference spectra found in the literature. While LMC spectrum is well documented, Wang et al. questioned the validity of the preceding LEDC synthesis method [Wang et al. *Nat. Chem.* (2019)], evidencing troubling resemblance between the FTIR spectrum of lithium ethyl mono-carbonate (LEMC) they prepared, and previous spectra reported as LEDC [Zhuang et al. *J. Phys. Chem. B* (2005)]. Doing so, they suggested that the SEI is made up of LEMC rather than LEDC, even though no clear evidenced formation mechanism was proposed. While the presence of given semi-carbonates have be evidenced is specific cases, the exact nature of the species present remains a matter of discussion in the general case. Our data on LTO shows the same strong bands at 1400 cm$^{-1}$ and 1300 cm$^{-1}$ as LEMC or initial reports of LEDC (Figure 6f), but the characteristic LEMC -OH band was not detectable within the accuracy of our experiment. (Supplementary Fig. 26). Additional work will be necessary to come up with a comprehensive model of semi-carbonate compositions.

## Supplementary – Assessing the repeatability of $A(t)$-$A(t_0)$ amplitudes

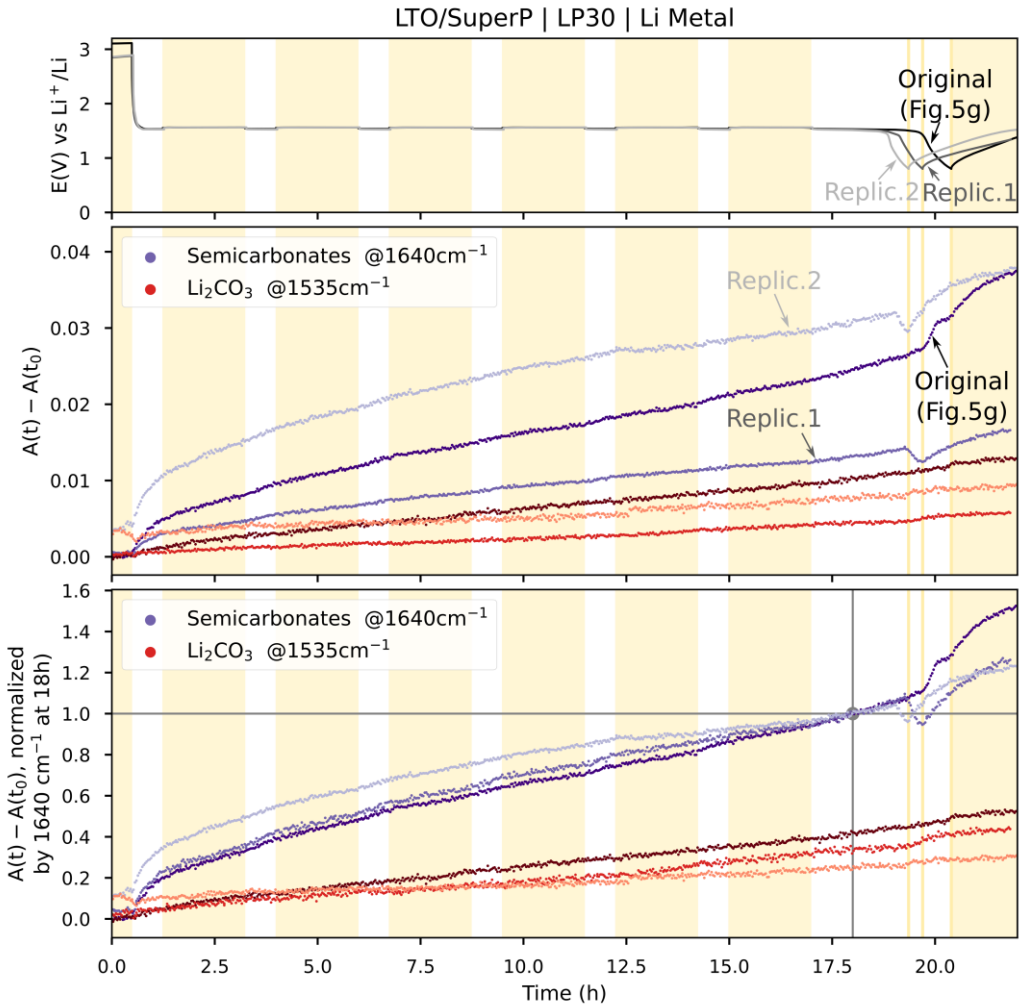


Supplementary Fig. 27. Comparison of GITT protocols of three LTO/SuperP|LP30|Li Metal cells, including the cell presented in Figure 5g. **Upper panel**, GITT cycling curve, OCV periods are represented in yellow. Timescale were shifted to align to the beginning of the first reduction. **Middle panel,** evolution of the two wavenumbers representative of semi-carbonates and $Li_2CO_3$. **Lower panel**, same curves, normalized by the value of absorbance at 1640 $cm^{-1}$ after 18h.

Three LTO/SuperP|LP30|Li Metal cells were assembled and cycled to evaluate the reproducibility of the spectra. While the three cells show very identical electrochemistry, it should be noted that significant intensity differences are observed between experiments, which we attribute to variations in sample preparation such as difference in fibre coverage, particle adhesion, and electrode cohesion permitting electronic conductivity. Designing more systematic deposition methods should improve the reproducibility of these intensities. However, once normalized, all these curves show similar trends.

Notably, they show a break in slope once leaving the 1.5V-insertion plateau, with decreased amount of semi-carbonates, which was also repeatedly observed on long cycling data (see Supplementary Fig. 31). We presume that these artefacts could be due to the formation of other SEI species, undetectable by mid-IR spectroscopy, but affecting the refractive index in the volume near the sensor surface and thus impacting the penetration depth of the evanescent wave.

## Supplementary - Commercial electrolyte reduction on LTO – Longer Cycling

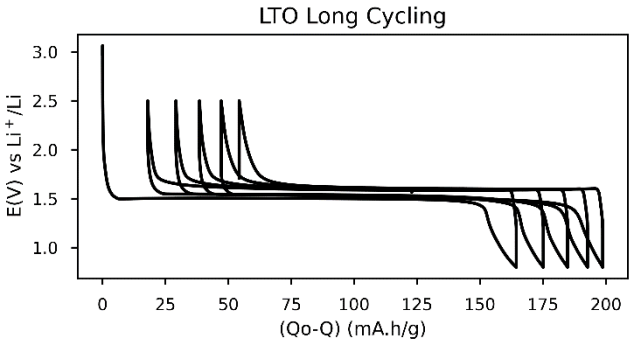


Supplementary Fig. 28. Voltage vs specific capacity for the long cycling LTO cell

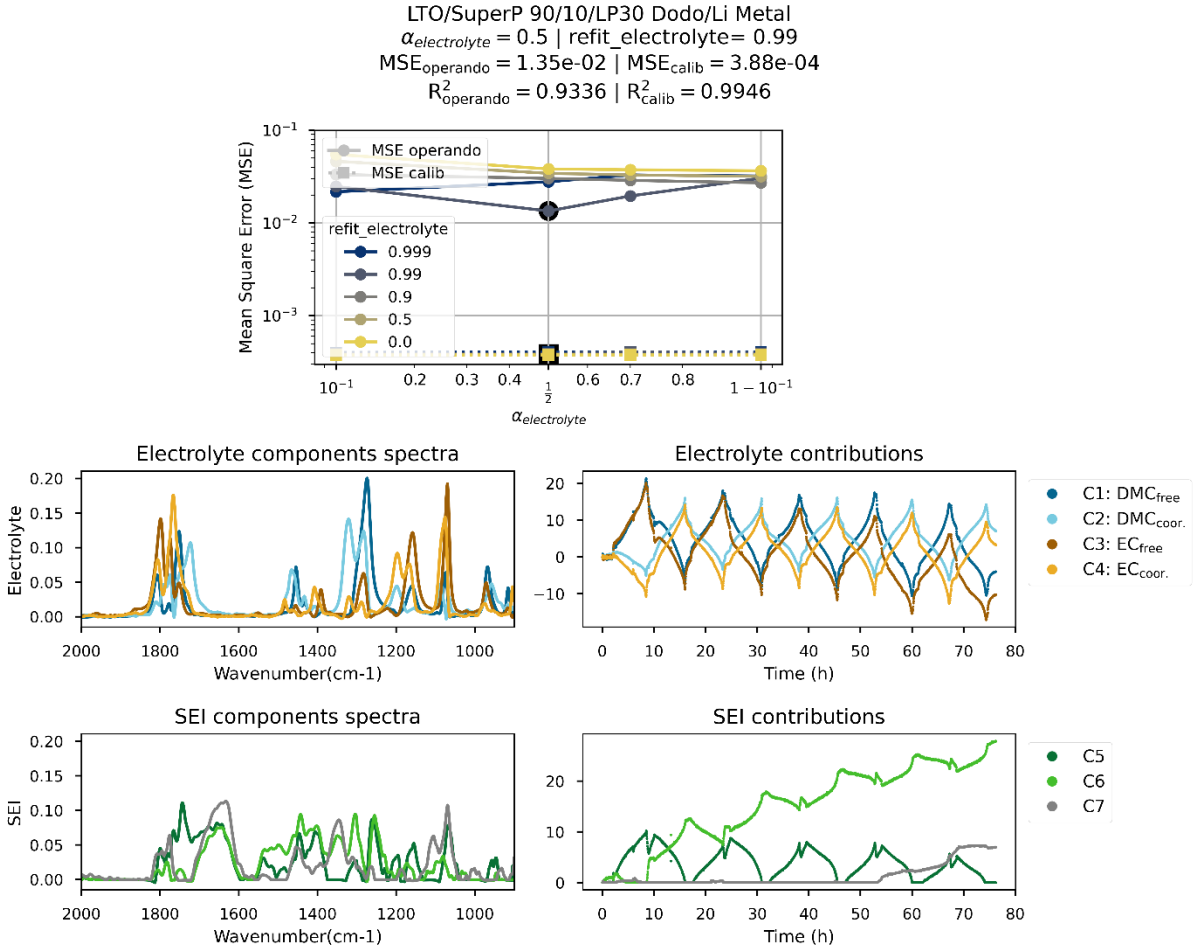


Supplementary Fig. 29. **Detailed MCR-ALS for the LTO/SuperP | LP30 | Li long cycling cell.** MSE of operando and calibration spectra (solid and dashed lines, respectively), for several values of $\alpha_{electrolyte}$ and electrolyte refitting parameter (upper panel). The decomposition reported in the main text is highlighted with black markers, and detailed on the four lower panels: spectra (left panels) and associated contributions (right panels) for electrolyte (middle panels) and SEI components (lower panels).

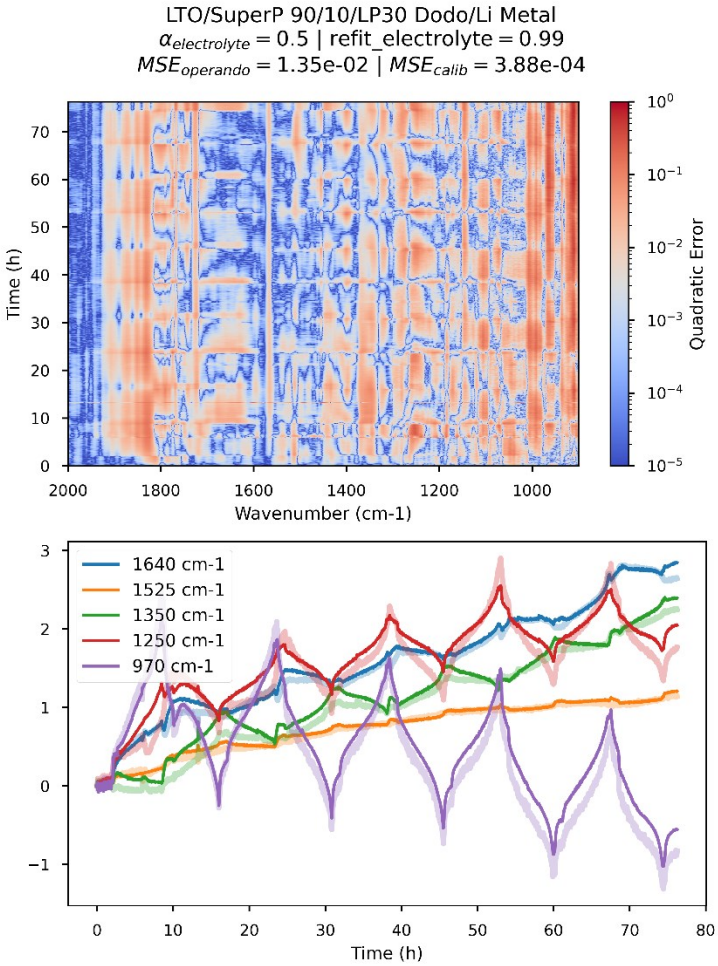


Supplementary Fig. 30. **Detailed MCR-ALS for the LTO/SuperP | LP30 | Li long cycling cell.** Quadratic error between operando data D and reconstructed from MCR-ALS ($CS^T$) (upper panel). Comparison of operando data D (transparent lines) and reconstructed data from MCR-ALS ($CS^T$) (solid lines) at selected wavenumbers.

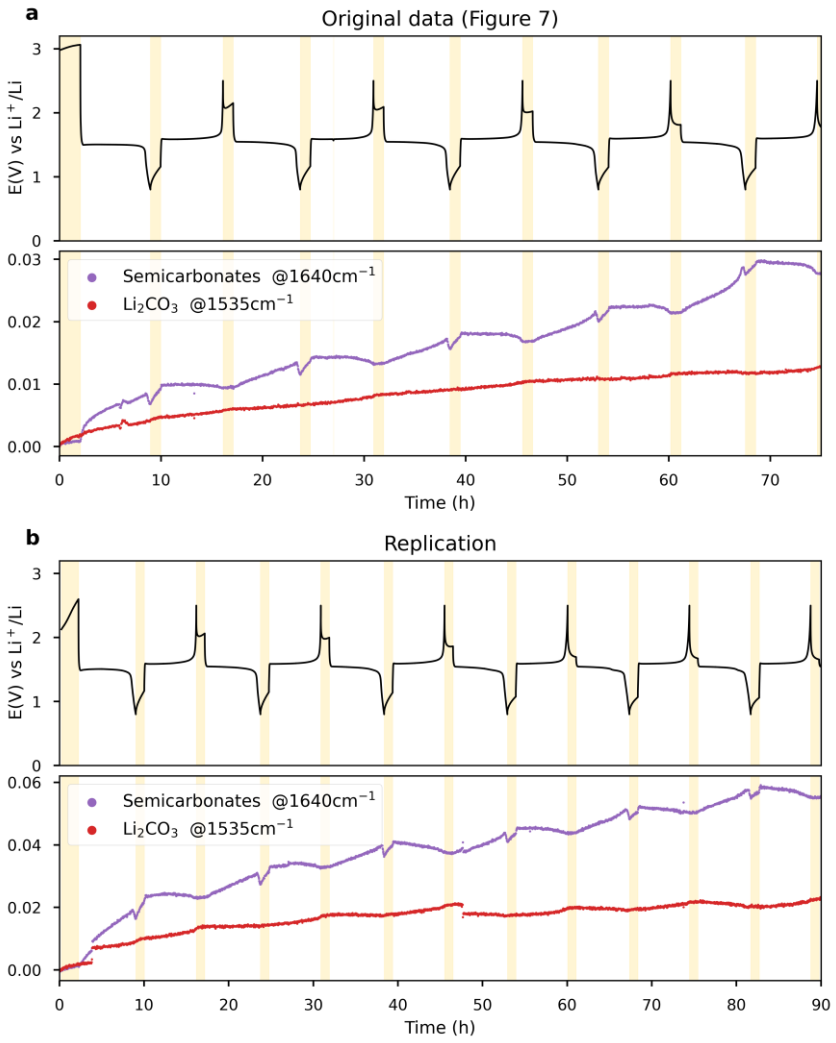


Supplementary Fig. 31. **Comparison of two long cycling protocols of LTO/SuperP|LP30|Li Metal cells** for **a,** the cell presented in main text of the paper, **b**, a cell assembled in identical conditions. Upper panel: GITT trace, OCV periods are represented in yellow; Lower panel: $A(t)$-$A(t_0)$ evolution for the two wavenumbers representative of semi-carbonates and $Li_2CO_3$. While the absolute absorbance vary with a two-fold between experiments, both curves show similar temporal evolution.

## Supplementary: Effect of carbon additives on the spectra

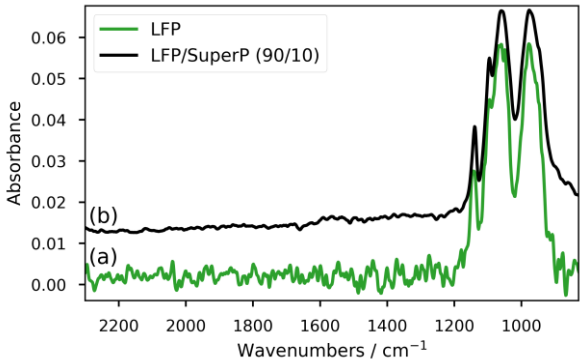


Supplementary Fig. 32. **Effect of carbon additive on spectra of a solid sample**. **a** IR-FEWS of LFP particles deposited on TAS fibre via ethanol dispersion. **b** IR-FEWS of LFP/SuperP particles mixture on TAS fibre, showing an increased baseline due to the carbon. In both cases, the background was acquired on a raw TAS fibre.